

Journal Pre-proof

Flow field distribution and overpressure characteristics inside the crew compartment of a truck-mounted howitzer under the effect of muzzle blast

Shengcheng Wei, Linfang Qian, Yadong Xu, Qiang Yin, Xinyu Xiong



PII: S2214-9147(24)00233-2

DOI: <https://doi.org/10.1016/j.dt.2024.09.008>

Reference: DT 1516

To appear in: *Defence Technology*

Received Date: 6 August 2024

Revised Date: 29 August 2024

Accepted Date: 19 September 2024

Please cite this article as: Wei S, Qian L, Xu Y, Yin Q, Xiong X, Flow field distribution and overpressure characteristics inside the crew compartment of a truck-mounted howitzer under the effect of muzzle blast, *Defence Technology*, <https://doi.org/10.1016/j.dt.2024.09.008>.

This is a PDF file of an article that has undergone enhancements after acceptance, such as the addition of a cover page and metadata, and formatting for readability, but it is not yet the definitive version of record. This version will undergo additional copyediting, typesetting and review before it is published in its final form, but we are providing this version to give early visibility of the article. Please note that, during the production process, errors may be discovered which could affect the content, and all legal disclaimers that apply to the journal pertain.

© 2024 China Ordnance Society. Publishing services by Elsevier B.V. on behalf of KeAi Communications Co. Ltd.

Flow field distribution and overpressure characteristics inside the crew compartment of a truck-mounted howitzer under the effect of muzzle blast

Shengcheng Wei^a, Linfang Qian^{a,b,*}, Yadong Xu^a, Qiang Yin^a, Xinyu Xiong^a

^aSchool of Mechanical Engineering, Nanjing University of Science and Technology, Nanjing 210094, China

^bNorthwest Institute of Mechanical and Electrical Engineering, Xianyang 712099, China

*Corresponding author: lfqian@njust.edu.cn

Journal Pre-proof

Flow field distribution and overpressure characteristics inside the crew compartment of a truck-mounted howitzer under the effect of muzzle blast

Abstract

The muzzle blast overpressure induces disturbances in the flow field inside the crew compartment (FFICC) of a truck-mounted howitzer during the artillery firing. This overpressure is the primary factor preventing personnel from firing artillery within the cab. To investigate the overpressure characteristics of the FFICC, a foreign trade equipment model was used as the research object, and a numerical model was established to analyze the propagation of muzzle blast from the muzzle to the interior of the crew compartment under extreme firing condition. For comparative verification, the muzzle blast experiment included overpressure data from both the flow field outside the crew compartment (FFOCC) and the FFICC, as well as the acceleration data of the crew compartment structure (Str-CC). The research findings demonstrate that the overpressure–time curves of the FFICC exhibit multi-peak characteristics, while the pressure wave shows no significant discontinuity. The enclosed nature of the cab hinders the dissipation of pressure wave energy within the FFICC, leading to sustained high-amplitude overpressure. The frame-skin structure helps attenuate the impact of muzzle blast on the FFICC. Conversely, local high overpressure caused by the convex or concave features of the cab's exterior significantly amplifies the overpressure amplitude within the FFICC.

Keywords: Truck-mounted howitzer; Muzzle blast; Flow field inside the Crew Compartment (FFICC); Overpressure characteristics; Flow-structure interaction

Flow field distribution and overpressure characteristics inside the crew compartment of a truck-mounted howitzer under the effect of muzzle blast

Abstract

The muzzle blast overpressure induces disturbances in the flow field inside the crew compartment (FFICC) of a truck-mounted howitzer during the artillery firing. This overpressure is the primary factor preventing personnel from firing artillery within the cab. To investigate the overpressure characteristics of the FFICC, a foreign trade equipment model was used as the research object, and a numerical model was established to analyze the propagation of muzzle blast from the muzzle to the interior of the crew compartment under extreme firing condition. For comparative verification, the muzzle blast experiment included overpressure data from both the flow field outside the crew compartment (FFOCC) and the FFICC, as well as the acceleration data of the crew compartment structure (Str-CC). The research findings demonstrate that the overpressure–time curves of the FFICC exhibit multi-peak characteristics, while the pressure wave shows no significant discontinuity. The enclosed nature of the cab hinders the dissipation of pressure wave energy within the FFICC, leading to sustained high-amplitude overpressure. The frame-skin structure helps attenuate the impact of muzzle blast on the FFICC. Conversely, local high overpressure caused by the convex or concave features of the cab's exterior significantly amplifies the overpressure amplitude within the FFICC.

Keywords: Truck-mounted howitzer; Muzzle blast; Flow field inside the Crew Compartment (FFICC); Overpressure characteristics; Flow-structure interaction

1. Introduction

A truck-mounted howitzer is a type of wheeled self-propelled artillery system consisting of artillery, ammunition, a wheeled military truck chassis, and information systems. It offers significant advantages in terms of lightweight design and high motility [1]. Given the escalating demand for rapid response in modern warfare and the maturity of automatic ammunition loading technology, it has become a natural progression for truck-mounted howitzers to efficiently execute firing tasks and swiftly withdraw from battlefields without requiring personnel to leave the cab. The muzzle of a truck-mounted howitzer is typically positioned in the frontal region of the truck. The distance between the muzzle and the crew compartment of a truck-mounted howitzer (CCTMH) is small in scenarios with low firing angles, as shown in Fig. 1. When the artillery fires, the high-speed and high-pressure muzzle blast is prone to generate overpressure with significant peak values on the surface of the CCTMH [2,3], subsequently causing intense pressure fluctuations inside the crew compartment, posing a serious threat to the safety of operators within the vehicle, as depicted in Fig. 1. Due to the lightweight design requirements of the CCTMH, measures such as significantly increasing the density of the frame, thickening the skin, and other methods to enhance the cab's anti-muzzle blast performance make it difficult to achieve a balance of various indicators for the CCTMH. Furthermore, the conventional approach of adjusting the design based on numerous shooting tests to find an optimal solution

would require significant human and material resources, making it unattainable within a limited timeframe. Therefore, it is imperative to thoroughly investigate the complete propagation path of the shock wave from the muzzle to the interior of the CCTMH. This research should encompass an analysis of the causes and distribution characteristics of overpressure within the flow field inside the crew compartment of a truck-mounted howitzer (FFICC) and identify key factors that influence its magnitude. Provide targeted guidance for the optimized design of anti-shock wave structures for the CCTMH, taking into account the internal flow field environment.

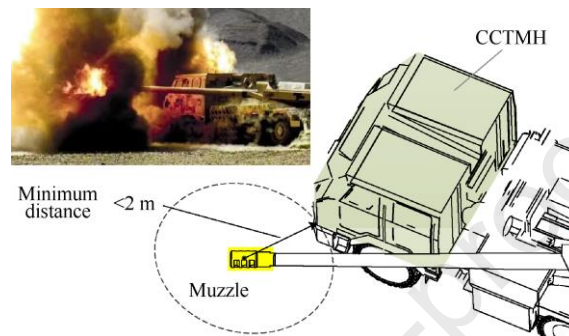


Fig. 1. Low firing angle condition of the truck-mounted howitzer.

The propagation and development of muzzle blast in the flow field outside the crew compartment of a truck-mounted howitzer (FFOCC) are determining factors for the formation of pressure waves in the FFICC. This process mainly includes three main stages: near-field of the muzzle, far-field of the muzzle, and structural coupling. The muzzle blast has a short duration and drastic parameter changes, coupled with the complex structure of the muzzle brake, making it very difficult to calculate and observe the FFOCC. To analyze the relevant issues of muzzle blast propagation, many scholars have conducted a large amount of research [4–21]: In the studies on the muzzle flow field considering the influence of the muzzle brake, Li and Zhang [9] illustrated the interaction of the blast waves released from the muzzle brake in detail and analyzed the mechanism of muzzle flash formation. They concluded that the interactions of the jet flow emanating from the lateral slots lead to more intense combustion in the primary stage of the muzzle flow. Another study conducted a numerical analysis of impinging flows generated by propellant gas released from the muzzle of a high-frequency launch system. By comparing the deformation results of the impingements at three distinct impact frequencies, this study demonstrated the influence of impact frequency on both damage effects and accumulation phenomena [10]. The research results of Wei et al. [3] indicate that the orientation of the muzzle brake's recoil orifice has a significant impact on the overpressure on the surface of the CCTMH. The impact of projectile motion on the muzzle blast is confined to its initial growth phase. In the relevant studies [14], Zhuo et al. [15] and Luo et al. [16] applied a dynamic overlapping grids approach to solve the muzzle flow field. Numerical investigations of the launch process of a base bleed projectile from the muzzle to free-flight stage have been performed successfully by Zhou and Luo et al. [15,16]. conducted a comparative study on the influence of three kinds of projectile nose shapes (flat, cone, and blunt) on the muzzle flow field. This study showed

that some wave processes, such as shock-shock interactions, separated flow generation, and the Richtmyer-Meshkov Instability, change significantly with the change in projectile shape. In the near-field region of the muzzle, the presence of the precursor flow field will have a certain impact on the formation and development of the muzzle flow field. Lei et al. [17] and Guo et al. [18] constructed two 3D computational models, one incorporating a precursor flow field and the other excluding it, and systematic shooting tests were conducted. The research results indicate that at a distance of about twice the caliber from the side of the muzzle, the pressure in the flow field considering the precursor flow approaches that without considering the precursor flow. In experimental testing, Chen et al. [19] established a comprehensive testing system for muzzle blast, analyzing the magnitude and distribution of naval gun muzzle blast and investigating the density of isobars at the muzzle during launches with high-temperature and low-temperature ammunition. Moumen et al. [20] proved the feasibility of the Particle Image Velocimetry technique in muzzle flow field analysis through meticulous experimental research.

Additionally, some scholars have integrated artificial intelligence technology with high-speed flow field and shock wave propagation research [22–26], providing new ideas for studying muzzle blast. Zhou et al. [27] incorporated artificial intelligence technology into the simulation of the muzzle flow field and developed an AI-based solution model for the muzzle flow field, significantly enhancing computational efficiency while maintaining comparable accuracy to CFD.

When large-caliber truck-mounted howitzers in active service around the world are fired, the operators are typically located in the open area behind the artillery, far from the cab. Consequently, current research on the impact of muzzle blast on the CCTMH is limited to the distribution of external shock wave overpressure and structural strength verification [3,28,29]. There are few studies currently available on the FFICC under the effect of muzzle blast. In the field of railway transportation, when a high-speed train passes through a tunnel, the interaction between the train and air generates significant fluctuations in tunnel pressure waves. These pressure waves causing pressure fluctuations within the carriage, ultimately impacting conductor and passenger comfort [30–34]. This problem encompasses the external flow field, internal flow field, and structural force field of the carriage. It exhibits significant theoretical similarities to the issue of FFICC influenced by muzzle blast in terms of load transfer processes, and formation reasons of pressure waves within the cab. Feng et al. [34] divided the problem of high-speed train carriages subjected to tunnel pressure waves into two stages. The first stage focused on the external flow field of the carriage, and the second stage on the internal flow field considering structural coupling. Utilizing the STAR-CCM+ Co-Simulations module, the interleaved coupling integral method (Loose Coupling) was employed to investigate pressure fluctuations within the flow field of a high-speed train carriage under varying external tunnel pressure waves. This research concept can also be extended to the investigation of FFICC under the influence of muzzle blast. However, there are notable distinctions between the propagation velocity, and pressure gradient of tunnel pressure waves and muzzle blast. Feng's proposed method, which solely captured pressure data from some representative points on the carriage's surface as the input of the load of the external flow field, cannot be directly applied to the

research of the overpressure load of surface-related muzzle blast on the CCTMH.

This study focuses on a large-caliber truck-mounted howitzer as the subject of investigation. By incorporating the aforementioned conclusions, a numerical model was constructed employing the simulation strategy of distribution modeling and joint calculation to accurately depict the complete trajectory of the shock wave propagation from the muzzle to the interior of the CCTMH under extreme firing condition (The elevation angle of the artillery barrel is 0° , and the azimuth angle is 25° to the left. Hereinafter abbreviated $0^\circ/-25^\circ$). The simulation obtained the development trend of shock wave overpressure in the FFOCC, structural acceleration of the crew compartment structure (Str-CC), and overpressure in the FFICC as functions of time under extreme firing angles. Meanwhile, a systematic firing experiment scheme was devised, encompassing both the FFOCC and the FFICC, as well as the structural response, to validate the accuracy of the numerical model. Through further analysis of numerical simulations and experimental results, this study discusses the causes and characteristics of overpressure in the FFICC and clarifies the key factors influencing this overpressure.

2. Numerical model

2.1. Description of the shock wave propagation and assumptions

The overpressure characteristics of the FFICC under the effect of muzzle blast represent a multi-physics coupling problem encompassing the FFOCC, the Str-CC, and the FFICC. A single numerical model struggles to simulate the complete trajectory of the shock wave propagation from the muzzle to the interior of the CCTMH. Additionally, several intricate factors must be taken into account during firing. The formation mechanism, energy magnitude, and propagation velocity of overpressure in the FFOCC and the FFICC exhibit significant disparities during firing. To facilitate research, the process of muzzle blast propagation from the muzzle to the interior of the cab is delineated into two distinct stages. The first stage is the formation of the FFOCC, during which high-temperature and high-pressure shock waves are generated at the muzzle. Due to the influence of the muzzle brake, truck body structure, and ground, a significant overpressure distribution ultimately develops on the surface of the CCTMH [3]. The second stage involves the FFICC and the Str-CC, where the Str-CC undergoes significant deformation due to external overpressure loads. This results in pressure fluctuations in the FFICC, ultimately leading to a distribution of large-amplitude overpressure within the cab. Considering the actual operating conditions of the CCTMH, this study assumed that the cab functions as an ideal enclosed chamber. The interaction of the muzzle blast overpressure, structural deformation, and other loads between the FFOCC and FFICC is achieved through the Fluid-structure interaction boundary on the external surface of the CCTMH (represented by 'Outside-FSI') and on the inner wall (represented by 'Inside-FSI'). As shown in Fig. 2.

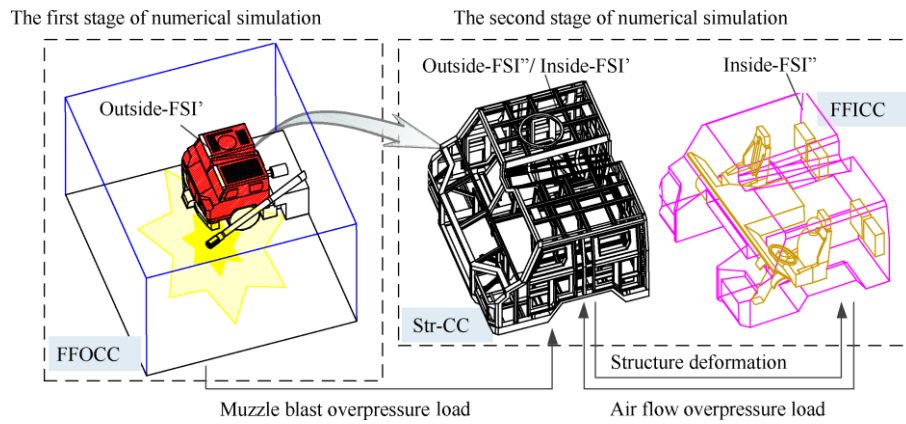


Fig. 2. The stage of propagation for muzzle blast.

In realistic conditions, the muzzle airflow generated by artillery firing is a gas-solid two-phase, multi-component fluid accompanied by chemical reactions [35]. The airflow immediately after exiting the barrel is also influenced by the precursor flow field, projectile movement, and other factors. Due to the complex flow field environment in the near-field area of the muzzle, it is necessary to reasonably simplify the muzzle airflow model. Zhuo et al. [35] compared the mixed muzzle jet containing solid particles and the ideal gas muzzle jet. The finding indicated that the developmental trajectory of the gas-solid mixed muzzle jet aligns closely with that of an ideal gas muzzle jet. Furthermore, it was observed that the velocity and arrival position of the muzzle blast formed by the two types of jets are nearly identical. Li et al. [14] used an ideal gas model to describe muzzle flow in the book *Intermediate Ballistics*. The results show that the impact of projectile motion on the muzzle powder jet is confined to its initial growth phase, with only localized perturbations observed in subsequent stages. In addition, Guo et al.'s research results indicate that at a distance of about twice the caliber from the side of the muzzle, the pressure in the flow field considering the precursor flow approaches that without considering the precursor flow [18].

Therefore, considering that the distance between the CCTMH and the muzzle investigated in this study exceeds ten times the caliber, there was no need to establish an excessively intricate mathematical model for the muzzle airflow. Assuming the CCTMH to be an ideal-closed system, it can be inferred that the gas composition within the cab is homogeneous. Based on the above analysis, to improve computational efficiency of the numerical model, the powder gas was approximated as an ideal gas. Factors such as gas-solid two-phase flow, multi-component flow, projectile motion, and precursor flow field were disregarded.

2.2. Model establishment and parameter settings

2.2.1. Physical model

The numerical model comprised three components: the computational domain for the FFOCC, the computational domain for the FFICC, and the model of the Str-CC. The extreme firing angle of the truck-mounted howitzer is $0^{\circ}/-25^{\circ}$. The size of the computational domain for the FFOCC at this firing angle is $9.4\text{ m}\times 8.3\text{ m}\times 5.6\text{ m}$. The numerical model of the FFOCC includes the artillery barrel, muzzle brake, main external features of the CCTMH, and other features such as the front bumper, truck beam, engine, and wheels, which significantly impact the FFOCC. Key elements of the cab were retained, including the gun barrel placement slot at the top of the cab, windshield glass,

lights, engine intake grille, and large sheet metal convex structures. For the FFOCC, the computational domain is a closed air domain enclosed by the cab structure, measuring approximately 2.4 m×2.8 m×1.5 m. The FFOCC model accurately represents the spatial shape of the cab and includes simplified components significantly impacting the FFOCC, such as seat and instrument installation supports. A simplified 1:1 scale half-body model was set up on the left driver's seat to simulate operator presence. The numerical model of the Str-CC comprised the frame structures, thin skin structures, window glazing, engine air intake grille, and escape window cover plate. as shown in Fig. 4

2.2.2. Grid model

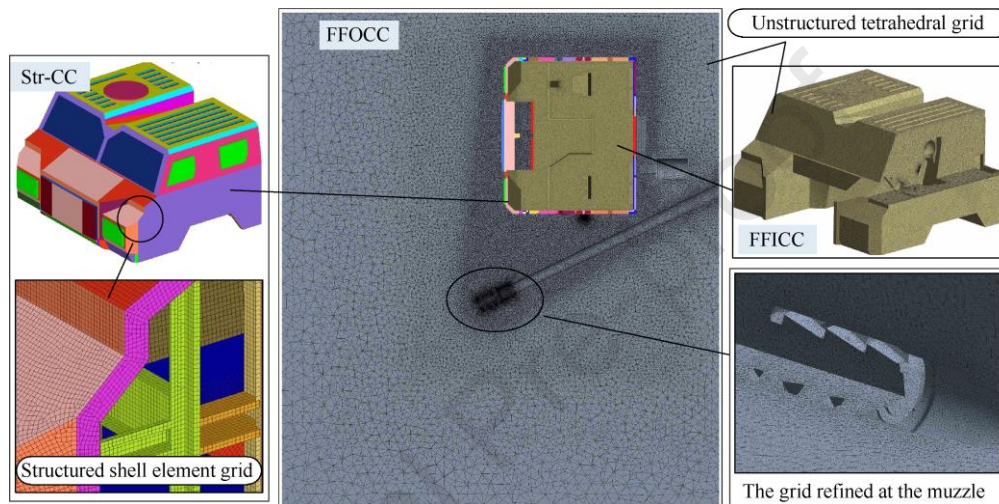


Fig. 3. Schematic diagram of grid model.

As shown in Fig. 3, unstructured grid technology with strong geometric adaptability was used to discretize the calculation domain of the FFOCC and the FFICC, while high-precision shell element structural grid technology was used for the Str-CC. To ensure the accuracy and convergence of the numerical calculation, local grid refinement was applied to the fluid grid surrounding the muzzle brake and between the muzzle and cab in the calculation domain of the FFOCC. For non-critical fluid regions distant from the muzzle and not impacting shock wave pressure distribution on the cab surface, a larger grid size was used to reduce computational load and optimize efficiency. The deformation of the Str-CC was responsible for transferring FFOCC loads to the FFICC. So, the dynamic grid method was used to handle changes in the computational grid of the FFICC caused by the motion of the Str-CC during the calculations. Therefore, a dynamic grid model with dense division was employed to accurately model the entire FFICC. The number of grid cells in each computing domain after model discretization is presented in Table 1.

Table 1

Number of grid in each computing domain.

Computing domain	Grid type	Grid quantity
FFOCC	Unstructured Tetrahedral grid	14221352
FFICC	Unstructured Tetrahedral grid (dynamic)	5023750

2.2.3. Governing equations and boundary conditions

In the numerical model, the gas flow was described by the inviscid three-dimensional Euler equations, with the governing equations as follows

$$\frac{\partial \mathbf{U}}{\partial t} + \frac{\partial \mathbf{f}}{\partial x} + \frac{\partial \mathbf{g}}{\partial y} + \frac{\partial \mathbf{h}}{\partial z} = 0 \quad (1)$$

where

$$\mathbf{U} = \begin{bmatrix} \rho \\ \rho u \\ \rho v \\ \rho w \\ e \end{bmatrix}; \quad \mathbf{f} = \begin{bmatrix} \rho u \\ \rho u^2 + p \\ \rho uv \\ \rho uw \\ u(e + p) \end{bmatrix}; \quad \mathbf{g} = \begin{bmatrix} \rho v \\ \rho vu \\ \rho v^2 + p \\ \rho vw \\ v(e + p) \end{bmatrix}; \quad \mathbf{h} = \begin{bmatrix} \rho w \\ \rho wu \\ \rho wv \\ \rho w^2 + p \\ w(e + p) \end{bmatrix}; \quad (2)$$

where ρ is the fluid density, p is the pressure, u is the velocity in the x direction, v is the velocity in the y direction, w is the velocity in the z direction. e is the total energy per unit volume which is defined as:

$$e = \frac{p}{\gamma - 1} + \frac{1}{2} \rho (u^2 + v^2 + w^2) \quad (3)$$

where γ is the specific heat ratio of gas.

The Density-Based solver and transient solution method were employed for both the FFOCC and FFICC. The Roe-FDS scheme was adopted, and the time marching method used implicit scheme to accelerate the convergence of numerical calculation. The flow control equation was discretized by the second-order upwind scheme.

The large-caliber truck-mounted howitzer described in this paper is mature equipment that has been mass-produced. The performance specifications, along with extensive firing tests, demonstrate that the Str-CC of the truck-mounted howitzer experiences only elastic deformation under the impact of the muzzle blast. Throughout the structural deformation process, there is a one-to-one correspondence between strain and stress, as implied by Hooke's Law:

$$\sigma_{ij} = \lambda \delta_{ij} \varepsilon_{ii} + 2G \varepsilon_{ij} \quad (4)$$

$$\lambda = \frac{\nu E}{(1 + \nu)(1 - 2\nu)} \quad (5)$$

$$G = \frac{E}{2(1 + \nu)} \quad (6)$$

where σ is the stress, ε is the strain, δ is the Kronecker- δ , λ is the lame constants, G is the Modulus of rigidity, E is the Young's modulus, ν is the Poisson's ratio.

The exterior skins of the CCTMH are made of bulletproof steel plates and common steel plates, while the frame structures are made of common steel. Additionally, the cab's windows and headlights are constructed with bulletproof glass. The parameters of the relevant materials can be found in Table 2.

Table 2

Types and parameters of materials.

Parameter	Bulletproof steel plate	Common steel plate	Bulletproof glass
Density/($\text{kg}\cdot\text{m}^{-3}$)	7850	7850	2500
Young's modulus/GPa	210	210	70
Modulus of rigidity/GPa	79.4	79.4	30
Poisson's ratio	0.3	0.3	0.24
Yield strength/MPa	800	245	—
Tensile strength/MPa	900	390	80 (Bending strength)

The flow field region in the numerical model contained three types of boundary conditions: Static Wall, Dynamic Wall, and pressure-inlet and pressure-outlet, as shown in Fig. 4. The load interaction between the FFOCC and FFICC was achieved through the Outside-FSI and Inside-FSI. In Fig. 4, Outside-FSI' and Outside-FSI'' denote the coupling interfaces in the FFOCC and Str-CC models, respectively, while Inside-FSI' and Inside-FSI'' indicate the coupling interfaces in the Str-CC and FFICC models. In the calculation domain of the FFOCC, the muzzle brake and barrel, the exterior surface of the CCTMH, the truck's structure involved in the calculation, and the ground are all defined as static wall boundaries. The remaining fluid domain boundaries were set as pressure-outlet boundaries. The pressure-inlet boundaries at the muzzle cross-section were described using a User-Defined Function (UDF). This UDF effectively captures the airflow change within the artillery bore during the after-effect period, while considering initial parameters of airflow at the muzzle based on internal ballistics. The FFICC is a closed calculation domain enclosed by the inner walls of the crew compartment, with Inside-FSI'' representing its boundary. The reflective walls in the FFICC, except the Inside-FSI, were all set as static wall boundaries.

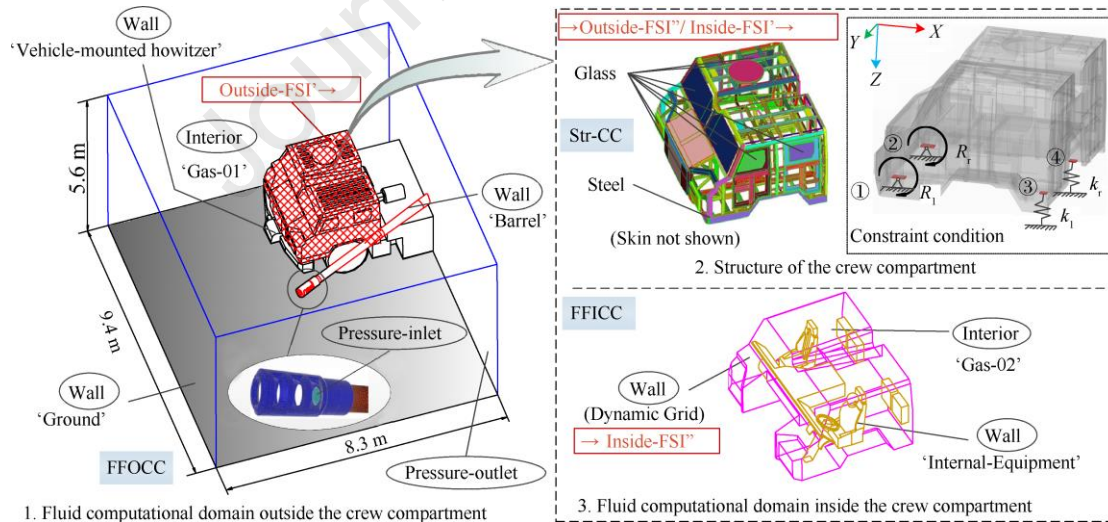


Fig. 4. Physical model and boundaries setting of computing domains.

The numerical model approximates the powder gas as an ideal gas. The specific heat of the FFOCC powder gas (Gas-01) is $1826.818 \text{ J}/(\text{kg}\cdot\text{K})$, with a molecular weight of $16.71 \text{ kg}/\text{kmol}$. The FFICC gas (Gas-02) is described using the ideal air model. The initial pressure value of the computational domain for both the FFOCC and FFICC was set to 101.325 kPa , while the initial temperature value was set to 300 K . The wall was assumed to be adiabatic,

and the temperature on the wall was taken from the mesh point temperature of the adjacent flow field. The muzzle airflow was initially set at a velocity of 940.3 m/s, with an initial temperature of 2297 K [3]. The muzzle exit time of the projectile in the numerical model calculation is considered to be instantaneous, defined as the initial time (t_0).

The numerical model includes four connection supports between the Str-CC and the truck beam, based on the actual fixed condition of the CCTMH, as shown in Fig. 4. The connecting seats ① and ② serve as hinged fulcrums along the y -axis, while the connecting seats ③ and ④ enable unrestricted movement along the x -axis and are flexibly constrained by a spring along the z -axis, with equal stiffness ($k_l = k_r$) and damping coefficient ($C_l = C_r$).

2.3. Model solving process

Based on the aforementioned two stages of muzzle blast propagation, the simulation solution strategy of distributed modeling and joint calculation was applied to achieve the Coupled simulation computation of the Str-CC, the FFOCC, and the FFICC under the effect of muzzle blast, the solution process is shown in Fig. 5. Firstly, the calculation of the FFOCC should be completed in the first stage, and the overpressure loads on the Outside-FSI should be extracted at each calculation step, and use it in conjunction with the overpressure loads on the Inside-FSI of the FFICC as the load input for the calculation of the Str-CC in the second stage. A bidirectional coupling calculation is conducted between the Str-CC and the FFICC in the second stage. The flow field calculation and finite element structural simulation iteratively advance through cross-interactions.

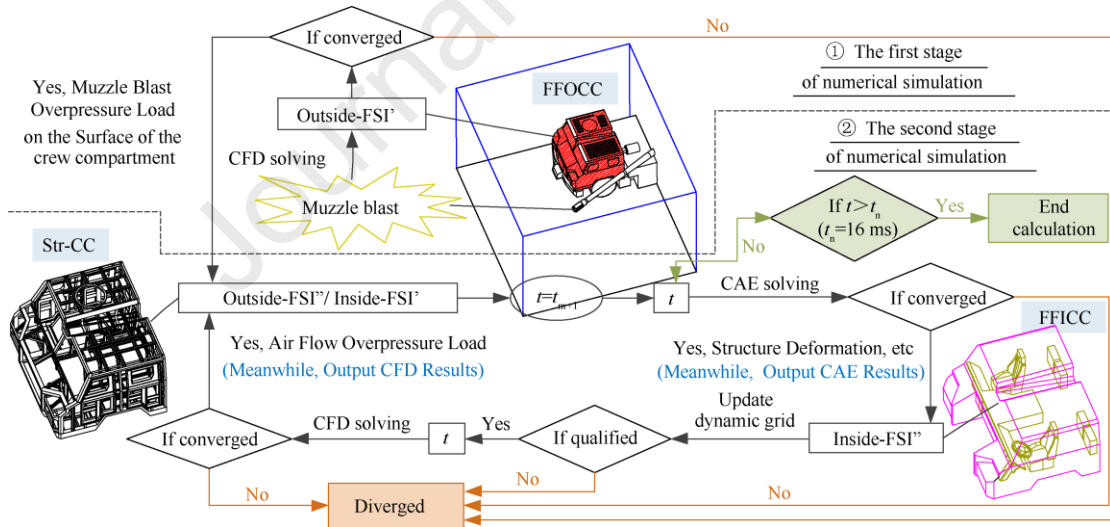


Fig. 5. The simulation solution process for muzzle blast.

3. Model verification

3.1. Plan for muzzle blast experiment

To validate the effectiveness and accuracy of the numerical model, a systematic firing experiment scheme was devised. This scheme includes measuring parameters such as the overpressure of the FFOCC and the FFICC, and the acceleration of the Str-CC, as depicted in Figs. 6 and 7. In the experiment, the truck-mounted howitzer utilized full-charge propellants to launch common projectiles, and the firing angle of the artillery was set at 0° - 25° . To

ensure the repeatability and accuracy of the results, three rounds of firing tests were conducted.

The equipment utilized in the experimental setup depicted in Fig. 6 can be categorized into two groups: essential equipment and data acquisition devices. The essential equipment includes computers, data acquisition instruments, cables, and brackets. The data acquisition devices are further classified into auxiliary measurement and direct measurement. The auxiliary measurement equipment consists of an infrared sensor, a high-speed camera, and an initial velocity measurement radar.

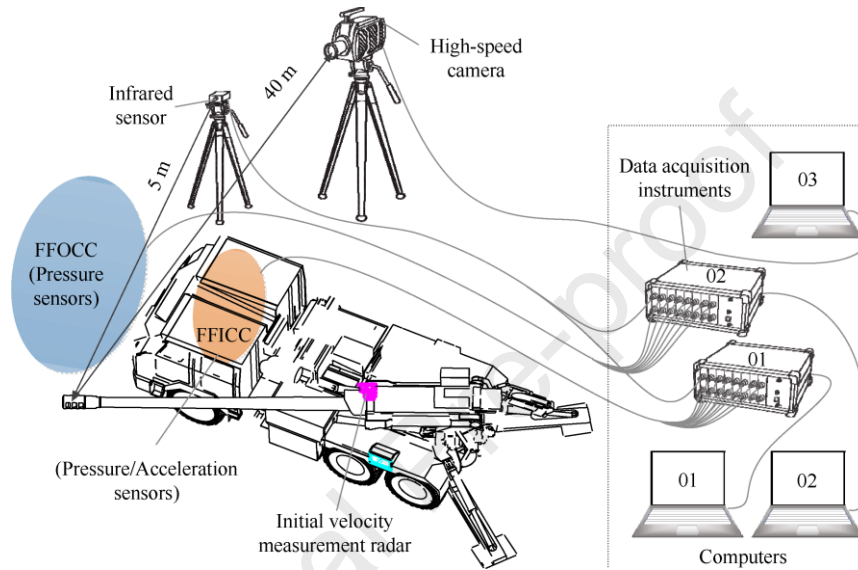


Fig. 6. Firing experiment scheme.

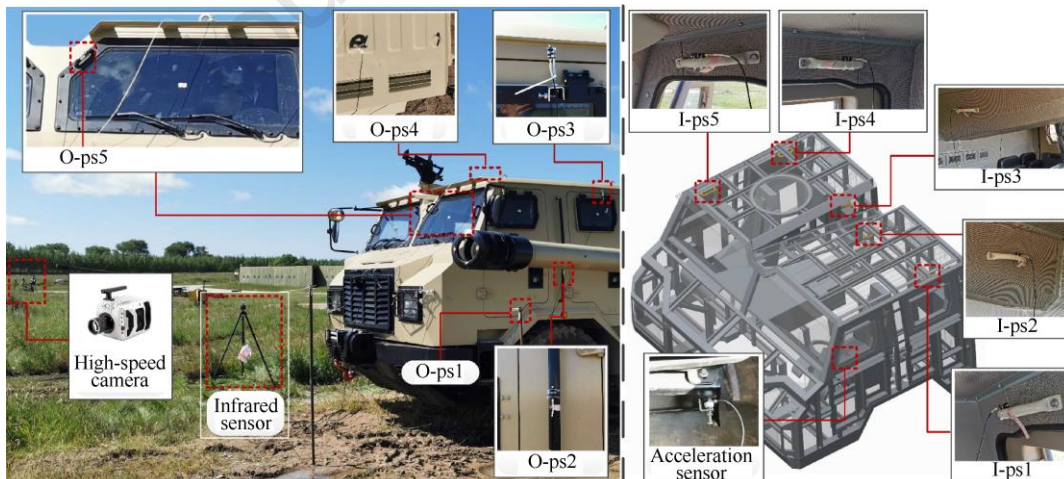


Fig. 7. The placements of sensors both externally and internally within the CCTMH.

The infrared sensor was positioned in front of the CCTMH, approximately 5 meters from the muzzle, connected to two data acquisition instruments. The moment when the infrared sensor detects the muzzle flame is considered the starting time (t_0) of the muzzle blast. The high-speed camera was positioned approximately 40 meters from the muzzle on the right side of the cab to observe the muzzle flame, smoke, and monitor the generation and propagation

of air compression waves during artillery firing. The initial velocity measurement radar of the truck-mounted howitzer was used to determine the muzzle velocity of the projectile. According to the Lagrange hypothesis, at the beginning of the after-effect period, the projectile velocity at the muzzle cross-section is equal to the muzzle powder gas velocity [14,36]. In addition to the aforementioned equipment, the Copper Ball Manometric Method was employed to record the maximum pressure value in the artillery bore during firing, comparing the consistency of results from the three firing tests and determining whether relevant firing parameters aligned with theoretical calculation values.

The direct measurement equipment comprises pressure sensors and an acceleration sensor for measuring the muzzle blast overpressure data of the FFOCC, the pressure wave overpressure data of the FFICC, and the acceleration data of the Str-CC. As shown in Fig. 7, five pressure sensors are installed on the outside of the crew compartment, labeled O-ps1–5 (maximum test range: 950 kPa). The O-ps1 sensor was positioned in the left front area of the cab to measure muzzle blast overpressure data near the muzzle without interference from the cab. Sensors O-ps2–5 were individually positioned on the left, front, and top sides of the CCTMH, facing the muzzle brake hole, which is the main impact area of the muzzle blast generated by firing. Inside the CCTMH, five pressure sensors labeled I-ps1–5 (maximum test range: 345 kPa) cover the main internal space area of the cab, and directly connected to the cab frame. The acceleration sensor (maximum test range: 100 g) was mounted on the support frame under the driver's seat, connected to the cab floor frame, and captures acceleration data along a unitary axis. Therefore, in accordance with its fixed orientation during experimentation, its measurement outcome is denoted as Acc-x. The parameters of some equipment and sensors used in the experiment are shown in Table 3.

Table 3

Parameters of equipment and sensors.

Equipment and sensors	Type	Sensitivity	range
Pressure sensor (FFOCC)	KISTLER 211B4	3.626 mV·kPa ⁻¹	1400 kPa
Pressure sensor (FFICC)	KISTLER 211B6	14.50 mV·kPa ⁻¹	340 kPa
Acceleration sensor	KISTLER 8763B100BB	57.46 mV·g ⁻¹	±100 g
High-speed camera	PHANTOM v2512	10000 fps	—

3.2. Analysis of experimental results

The muzzle velocity of projectiles (v_0) and maximum bore pressure (p_0) exhibited high consistency throughout the three rounds of firing tests, and the relative error compared to the theoretical calculation values is only 0.15% and 0.97%.



Fig. 8. The comparison of muzzle flame and smoke during the firing experiment.

During the experiment, due to a malfunctioning sensor and a loose connection cable, sensor I-ps2 did not obtain data. Additionally, sensor O-ps2 only recorded shock wave overpressure data during the initial 14 ms of the first and second firing tests. The detailed experiment results are presented in Table 4 and Figs. 9–11. The high-speed camera captured the flame and smoke at the muzzle during firing tests, as shown in Fig. 8. The first firing test, being a warm artillery firing, had issues such as low temperature in the gun barrel. It was clearly observed in the early stages of the first firing test that the muzzle was much more obscured by gunpowder smoke than in the two subsequent firing tests at the same moment. Consequently, the initiation time of the muzzle blast recorded by the infrared sensor is delayed in the first firing test, leading to an earlier detection of the muzzle blast response by each sensor compared to the other two firing tests, as illustrated in Figs. 9–11.

The maximum peak overpressure measured by each pressure sensor in both the FFOCC and FFICC exhibits a high level of consistency across all three firing experiments, as illustrated in Table 4. Moreover, the overall trend in overpressure development measured by the three parallel experiments remains consistent, as depicted in Figs. 9 and 10. The Acc-x-time curve obtained from the test is illustrated in Fig. 11. Similar to the overpressure-time curve, a high level of consistency is observed among the Acc-x-time curves measured by the three tests. The experimental results indicate that the peak value of the actual transient overload at the installation structure of the acceleration sensor, under the effect of the muzzle blast, exceeds 100 g. This surpasses the measurement range of the employed acceleration sensor in the experiment, resulting in an evident peak clipping phenomenon observed in the measured acceleration data. In short, the results of the three firing tests consistently and accurately depict the temporal development of overpressure in the FFOCC and FFICC, as well as the acceleration of the Str-CC under extreme firing condition.

3.3. Verification of the accuracy of simulation results

The experimental results indicate that the maximum peak value of overpressure in both the FFOCC and FFICC occurs within approximately 15 ms after the generation of the muzzle blast. Based on this phenomenon, the simulation calculation time for the numerical model was set at 16 ms to minimize unnecessary resource consumption while ensuring efficient computational performance. Additionally, the time step was adjusted to align with the sampling frequency of the test, which was set at 1×10^{-6} s. The measuring points corresponding to each sensor in the experiment were set in the numerical model to facilitate a direct comparison with the firing test results. The

comparison between the numerical calculation results and the experimental measured results at each measuring point is presented in Table 4 and Figs. 9–11.

Table 4

Comparison of the peak overpressure between simulation results and experiment results.

Sensors	Peak overpressure at each measuring point (within 16 ms)/kPa					Relative Error (Sim - \bar{V})
	Simulation	Experiment				
		V1	V2	V3	\bar{V}	
O-ps1	170.93	147.81	165.94	170.27	161.34	5.94%
O-ps2	154.73	158.21	153.09	--	155.65	0.59%
O-ps3	104.83	92.18	101.93	106.24	100.12	4.70%
O-ps4	67.45	58.24	65	66.12	63.12	6.86%
O-ps5	290.52	291.95	294.55	260.83	282.44	2.86%
I-ps1	3.38	2.96	4.08	3.45	3.50	3.43%
I-ps2	4.29	--	--	--	--	--
I-ps3	5.78	6.57	6.09	6.41	6.35	8.98%
I-ps4	6.01	5.15	5.31	5.30	5.25	14.41%
I-ps5	3.36	2.82	2.67	3.76	3.08	9.09%

Note: '--' Indicates that no valid data is available.

The relative errors between the simulation and test results for the maximum peak value of shock wave overpressure (i.e., the first peak value) at each test point in the FFOCC under extreme firing condition are all below 7%, as shown in Table 4. Additionally, Fig. 9 illustrates a high consistency between the shock wave overpressure-time curves of the simulation results and experimental results.

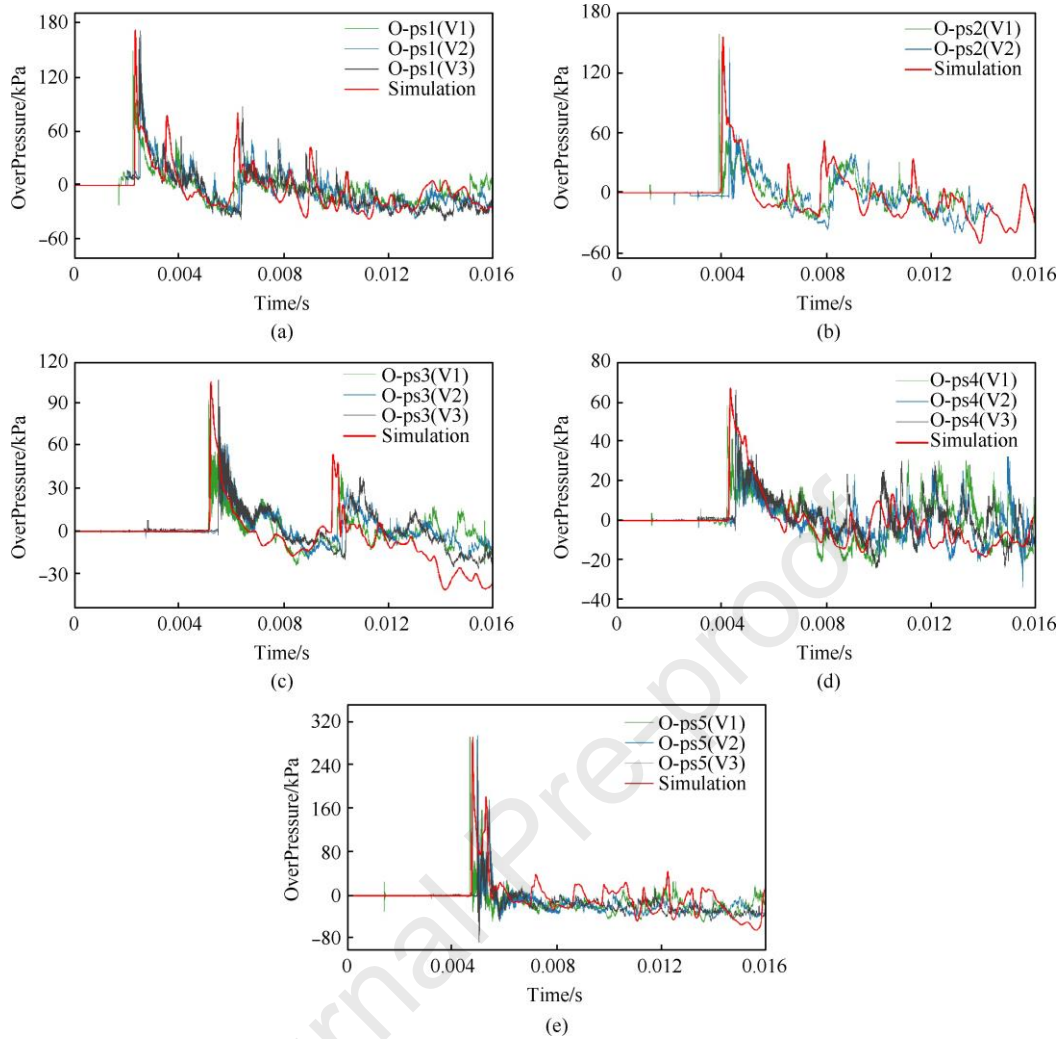


Fig. 9. Comparison of experimental and numerical overpressure-time curves of the FFOCC. (a) O-ps1; (b) O-ps2; (c) O-ps3; (d) O-ps4; (e) O-ps5.

Unlike the FFOCC, the muzzle blast indirectly acts on the FFICC through the vibration and deformation of the Str-CC. The establishment of the FFICC numerical model necessitates considering factors such as the FFOCC, Str-CC and its constraints, the characteristics of the FFICC, and other influential variables. However, it is important to note that incorporating these constraints may lead to the further accumulation of errors in the FFICC numerical model. Therefore, compared to the FFOCC, the errors between the simulated values of measuring points in the FFICC and the experimentally measured values are larger, as presented in Table 4.

The accuracy of Str-CC simulation results is a prerequisite for evaluating the accuracy of the FFICC numerical model. Therefore, the degree of agreement between the Acc-x model and experiments needs to be carefully considered. Due to limitations in the range of acceleration sensors, the comparison of Acc-x peak values between testing and numerical calculation cannot serve as a direct indicator for assessing the accuracy of the simulation model. However, Fig. 11 demonstrates that the Acc-x-time curve obtained from simulation calculations exhibits a high level of consistency with the observed pattern in experimental tests. This suggests that the Str-CC simulation is accurate. Meanwhile, the peak value of overpressure in the flow field simulation results at each point of the FFICC is highly

consistent with the measured results, with a relative error of less than 15%, as shown in Table 4. Moreover, the simulated trend of the FFICC overpressure curves over time is in excellent agreement with the experimental values, as illustrated in Fig. 10.

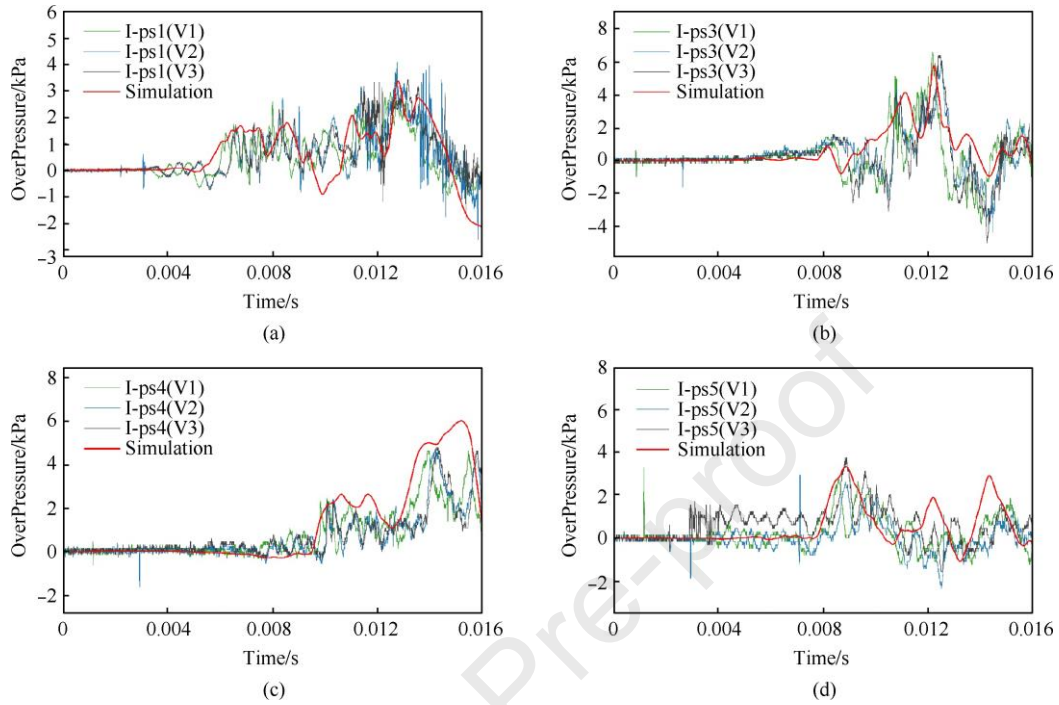


Fig. 10. Comparison of experimental and numerical overpressure-time curves of the FFICC. (a) I-ps1; (b) I-ps3; (c) I-ps4; (d) I-ps5.

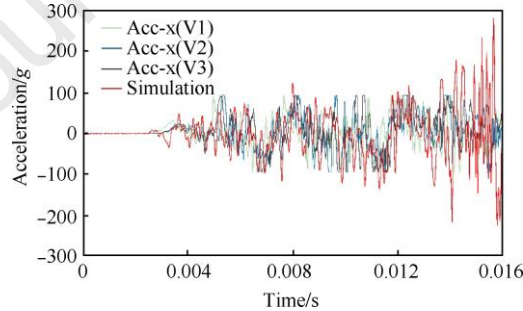


Fig. 11. Comparison of experimental and numerical Acc-x-time curve of Str-CC.

To summarize, the rationality and effectiveness of the numerical model are verified by comparing the simulation results and experiment results at each measuring point for both FFOCC and FFICC overpressure, as well as Str-CC acceleration. The numerical model accurately simulates the complete path of shock wave propagation from the muzzle to the interior of the CCTMH under extreme firing condition.

4. Results and discussion

4.1. Distribution and characteristics of overpressure of the FFICC

The artillery barrel is positioned lower than the top plane of the CCTMH under the extreme firing angle (0° - 25°). To visually analyze the formation and development of overpressure in the FFOCC and FFICC, color

nephograms depicting shock wave propagation from the muzzle to inside the cab are drawn on the XY plane of the muzzle, as shown in Figs. 12 and 13. The XY plane is aligned with the height of the personnel's chests within the cab.

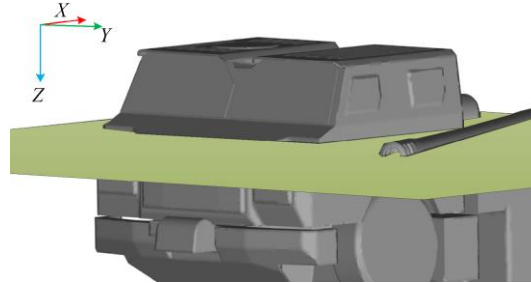


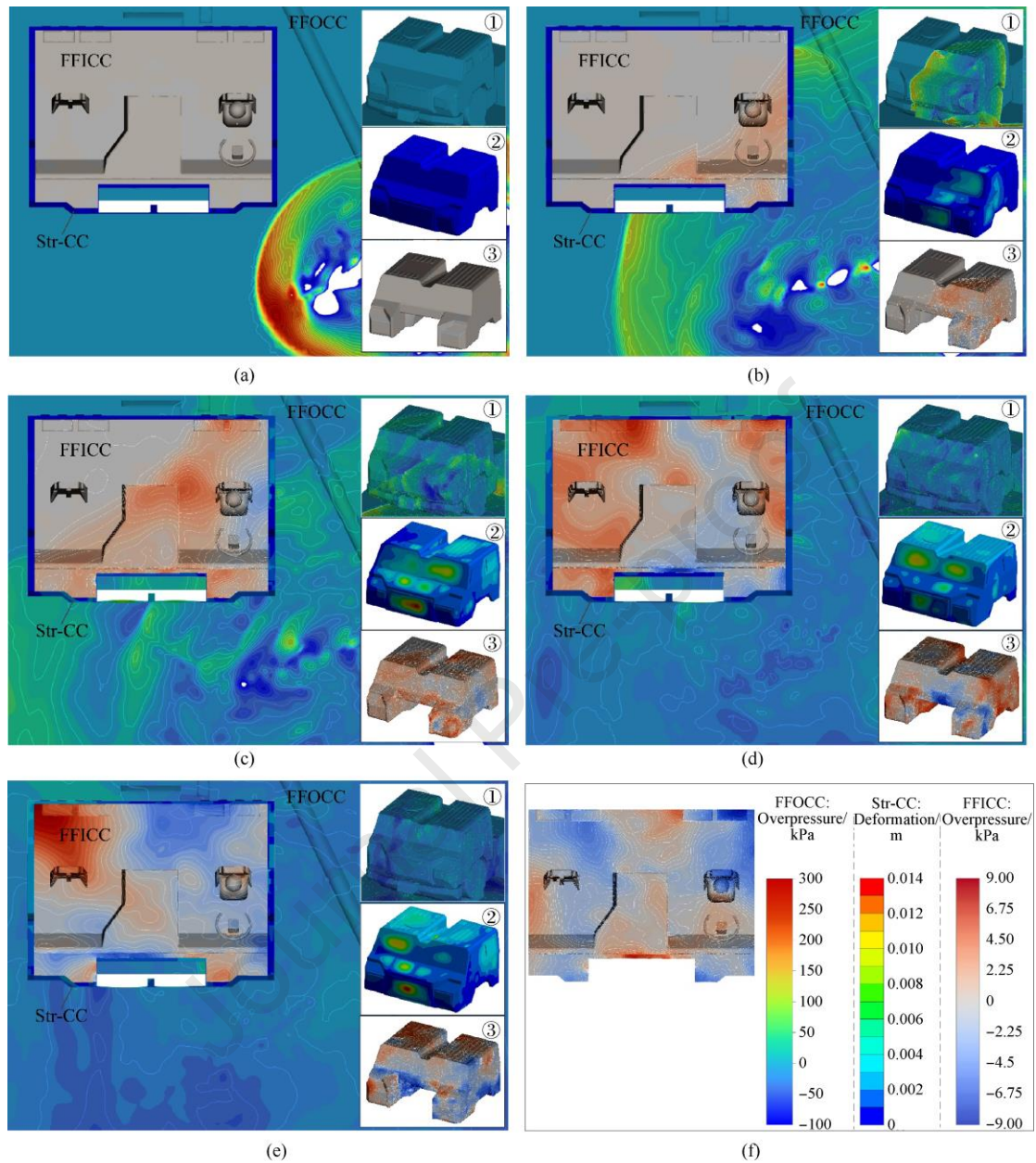
Fig. 12. XY plane of the muzzle.

The muzzle blast propagates in the FFOCC after its generation, as depicted in Fig. 13(a). At about 2.1 ms, the leading edge of the shock wave reaches the area where the front and left sides of the CCTMH meet. By approximately 5.3 ms, the muzzle blast induces rapid deformation of part of the cab structure, resulting in internal disturbance in the FFICC and simultaneous generation of a pressure wave. These structures are located on the left side of the front wall of the cab, as well as on both the left wall of the cab and the left front side of the top wall of the cab. Simultaneously, the shock wave reflecting off the ground (hereinafter referred to as the "ground-reflected wave") reaches the lower left region of the front of the cab, as shown in Fig. 13(b)-①. During the forward propagation of pressure waves, a significant overpressure distribution forms, as depicted in Fig. 13(b). It is evident that the pressure wavefront of the FFICC significantly lags behind the shock wavefront of the FFOCC due to attenuation caused by the Str-CC.

After 8 ms, the muzzle blast have covered most regions of the external surface of the cab. The overpressure value of the shock wavefront significantly decays during this period, and a wide low-pressure area is generated behind the wavefront on the exterior surface of the cab. Consequently, the region with high overpressure values of the FFICC gradually shifts from the left front side of the cab to the right rear side. At the same time, the ground-reflected wave causes the pressure wave of the FFICC to generate a new round of overpressure distribution in the left front area inside the cab. This results in negative pressure of the FFICC appearing only in a small area on the left side of the driving position, as depicted in Fig. 13(c).

The surface outside the cab has been fully covered by the muzzle blast after about 11.3 ms. At this point, the external surface of the cab is predominantly under negative pressure, except for the shock wavefront area, as depicted in Fig. 13(d)-①. Meanwhile, the pressure wavefront of the FFICC reaches the right and rear walls inside the cab. The maximum value of the pressure wave overpressure is still increasing due to wall reflections, pressure superposition, and hysteresis in the pressure changes of the FFICC. During this time, the regions exhibiting high overpressure values of the FFICC are predominantly concentrated on the right side of the cab, while a small area of overpressure is observed on its left rear side due to ground-reflected waves. Additionally, a negative-pressure region

can be identified between these two areas, as depicted in Fig. 13(d).



①: OverPressure on the Outside-FSI; ②: Total Deformation of the Str-CC; ③: OverPressure on the Inside-FSI

Fig. 13. The formation and distribution of overpressure of the FFOCC and FFICC. (a) 2.1 ms; (b) 5.3 ms; (c) 8.0 ms; (d) 11.3 ms; (e) 13.5 ms; (f) 16.0 ms.

After 13.5 ms, the overpressure value of the muzzle blastfront significantly decreases and continues to propagate toward the far field at the right rear of the cab. The external surface of the cab is predominantly characterized by negative pressure. During this period, only the region on the right rear side inside the cab exhibits high overpressure values. At this region, the pressure waves of the FFICC collide and superimpose with each other, resulting in a maximum peak overpressure of approximately 8.7 kPa on the XY plane of the muzzle inside the CCTMH, as depicted in Fig. 13(e). On the same plane, an area in the left rear region of the cab experienced a

maximum negative pressure with a peak value of around -8.92 kPa.

For a longer period after 13.5 ms, the muzzle blast continues to propagate toward the far field. The impact of the FFOCC overpressure on the cab Str-CC gradually diminishes. The peak overpressure of the FFICC continuously fluctuates during the propagation, collision, and fusion of the pressure waves. However, its overall magnitude exhibits a steady decrease and tends to stabilize.

As shown in Fig. 13, the peak overpressure at the boundary of the FFICC is only a fraction of the shock wave overpressure on the exterior surface at the same position, due to attenuation caused by the Str-CC. Take the symmetrically arranged measuring points O-ps3 and I-ps1 (as shown in Fig. 14) within and outside the cab structure as an example. The numerical calculation results demonstrate that from O-ps3 (104.83 kPa) to I-ps1 (3.38 kPa), the peak overpressure value attenuates by 96.78%, while the experimental data shows 96.5%. It should be noted that both measuring points are not very close to the cab structure. Therefore, the attenuation data of peak overpressure is generated due to the combined action of structural damping and increased distance. Meanwhile, in comparison to the FFOCC, the overpressure-time curve of the FFICC also demonstrates multi-peak characteristics. However, the pressure wave lacks significant discontinuity, and the changes in overpressure values of the FFICC remain relatively moderate over time, as illustrated in Fig. 14.

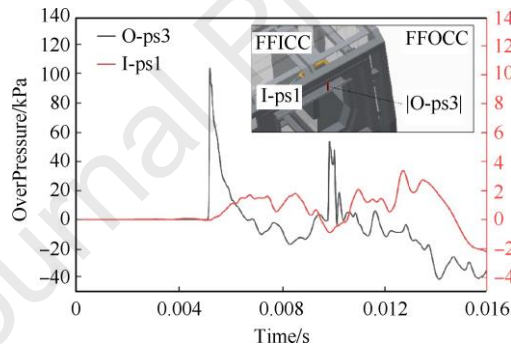


Fig. 14. Overpressure-time curves at measuring point O-ps3 and I-ps1.

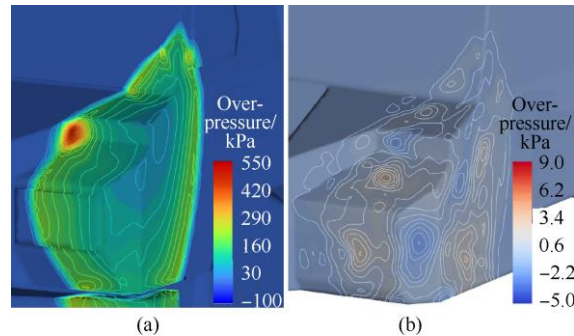


Fig. 15. Nephogram of overpressure (2.88 ms). (a) Outside-FSI; (b) Inside-FSI.

The CCTMH is constructed using a frame-skin structure, as shown in Fig. 4. The skins exhibit varying stiffness levels under the support of the frame: the skin near the frame demonstrates strong stiffness, while the skin at the center of the frame interval exhibits relatively weaker stiffness. Consequently, the skin deformation amplitude at the center of the frame interval is maximized when exposed to muzzle blast load. The resulting isobars of the pressure

wave overpressure nephogram on the boundary of the FFICC (Inside-FSI) exhibit multiple scattered central circular distributions, differing from those observed on the exterior surfaces of the CCTMH (Outside-FSI), as illustrated in Fig. 15. This suggests that the frame-skin structure can effectively disperse the muzzle blast load and mitigate the peak value of overpressure of the FFICC, but it also complicates the propagation trace of pressure waves.

4.2. Influencing factors of overpressure distribution within the CCTMH

4.2.1. Impacts of exterior surface shape and structural stiffness of the CCTMH

The exterior shape of the CCTMH is complex due to spatial limitations, equipment installation requirements, and other factors. Additionally, the external surfaces of the CCTMH feature numerous protruding or recessed structures such as windshields, windows, lights, engine intake grilles, handlebars, certain molding structures, and slots for gun barrel positioning.

The variation of the maximum overpressure on the Outside-FSI at each time point is illustrated in Fig. 16. The red dashed line represents the ideal exponential decay curve of shock wave overpressure with increasing distance. Apart from the 400 kPa overpressure formed when the muzzle blast reaches the joint region of the front side and left side of the cab around 2.3 ms, subsequent maximum overpressure values on the exterior surface of the cab are all generated at the convex or concave features. This is because the presence of these features disrupts the original exponential attenuation trend of shock wave overpressure on the external surface of the CCTMH.

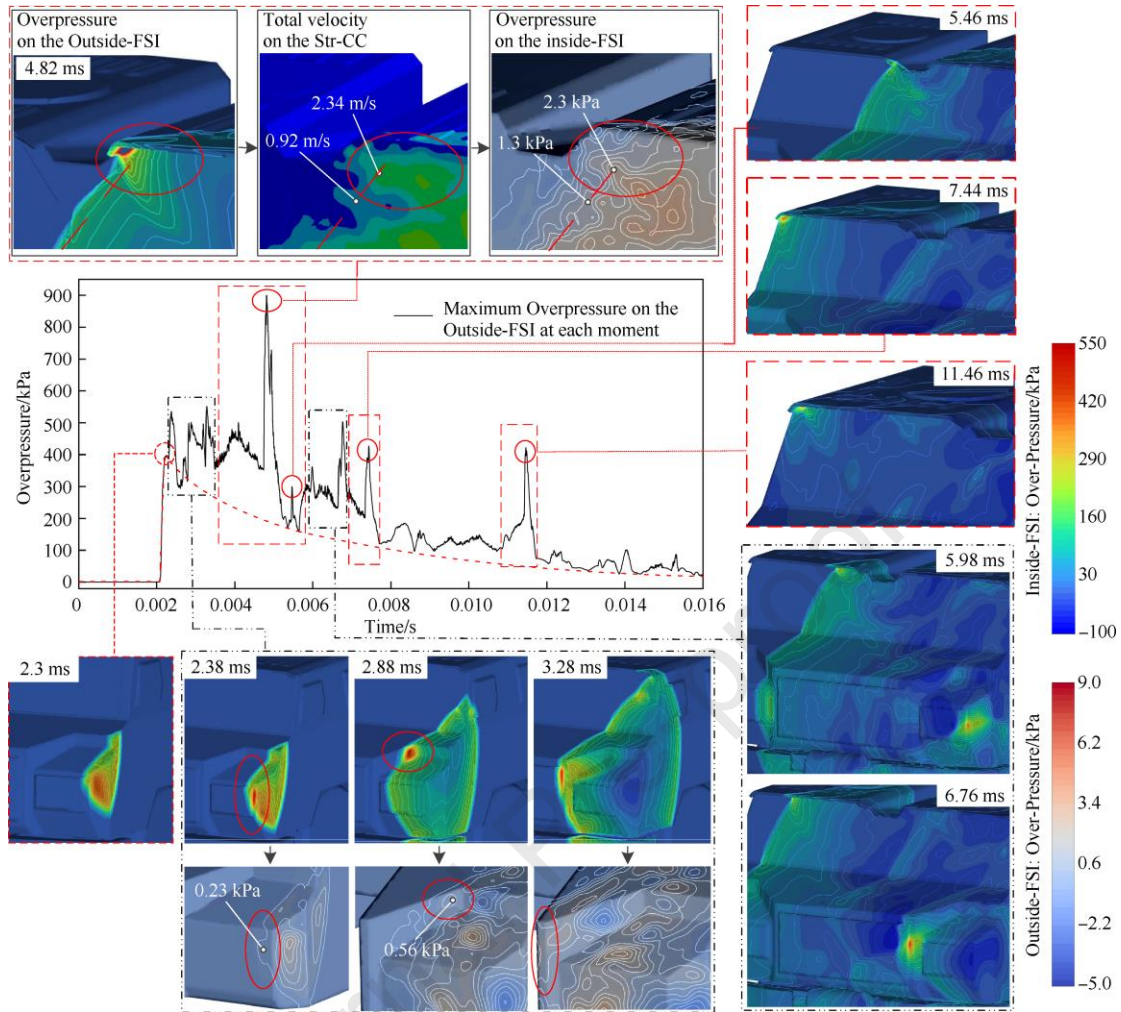


Fig. 16. Impacts of the external structure of CCTMH on the generation and evolution of shock wave overpressure.

The overpressure-time curve (as shown in Fig. 16) illustrates that the muzzle blast and the ground-reflected wave successively form multiple overpressures with amplitudes exceeding 500 kPa at various locations. These formations occur at specific places and times, including the left edge of the front cab headlight (2.38 ms/5.98 ms), the skin corner area above the headlight (2.88 ms/-), and the left edge of the engine intake grille (3.28 ms/6.76 ms). The maximum overpressure values of the shock wave on the exterior surface of the CCTMH are observed in the included angle regions formed by the windshields and the convex structure above them (as shown in Fig. 7) during time intervals ranging from 3.48 ms to 5.65 ms, 6.87 ms to 7.71 ms, and 10.86 ms to 11.72 ms. At about 4.82 ms, the shock wave overpressure on the Outside-FSI forms at the concave corner to the right of the bulge above the left windshield, reaching close to 900 kPa. The maximum overpressure on the Outside-FSI once again exceeds 420 kPa as the ground-reflected wavefront reaches the right concave corner of the included angle region above the right windshield at about 11.46 ms.

The local high-pressure generation of the shock wave is a gradual process. Therefore, even though the pressure wave overpressure on Inside-FSI has a certain lag compared with that on Outside-FSI, the overpressure cloud map of Inside-FSI can still be considered an accurate reflection of the influence trend of Outside-FSI on FFICC. The

structures that result in extreme overpressure values on the external surface of the cab are listed in Table 5. Among these structures, the lights and engine intake grille are external mounting structures of the CCTMH that can be removed. The glass used for the lights is a small-sized bulletproof glass with high rigidity, while the frame structure surrounding the mounting seat of the lights on the cab is densely constructed and exhibits significant stiffness. As a result, it becomes difficult for the muzzle blast overpressure to cause any detrimental deformation to these structures. Although the overpressure at the left edge of the headlight exceeds 500 kPa, the overpressure at the corresponding position of the FFICC is only 0.23 kPa, as evidenced by the 2.38 ms nephogram (as shown in Fig. 16). The primary structure of the engine intake grille is located in the FFOCC, and both sides are not directly connected with the FFICC. Therefore, the impact of overpressure exceeding 500 kPa generated at the left edge of the grille at 3.28 ms on the FFICC can be considered negligible. There is a concave corner region, consisting of three pieces of skin attached to the skeleton, which is part of the CCTMH structure located above the right of the left light. The structure itself and the surrounding structures have a high degree of rigidity. At 2.88 ms, Although the muzzle blast overpressure generated in this region approximately 500 kPa, the overpressure at the corresponding position of the FFICC is only 0.56 kPa, as shown in Fig. 16.

Table 5

The impact of structural features of the cab's exterior surface on the overpressure of the FFICC.

Exterior structures of the CCTMH that resulting in significant overpressure	Structural characteristics				Impact on the overpressure of the FFICC
	Structural type	Stiffness of itself	Whether it is directly connected to Inside-FSI	Stiffness of the surrounding structures	
Left light	External mounting structure	Strong	Yes	Strong	Slight (0.23 kPa, 2.38 ms)
Engine intake grille	External mounting structure	Weak	No	Strong	Ignored
The included angle region of the skin above the left light	Structure of the CCTMH itself	Strong	Yes	Strong	Slight (0.56 kPa, 2.88 ms)
The convex structure above the indshield	Structure of the CCTMH itself	Strong	Yes	Weak	Significant (1.3 kPa→2.3 kPa, ↑1 kPa, 4.82 ms)

The convex edge structure above the windshield is part of the CCTMH itself, which is much higher than the windshield plane. This structure and the windshield plane constitute a large included angle region toward the muzzle brake hole. Both the muzzle blast and ground-reflected wave generate high-pressure regions with large overpressure values in this included angle region, as depicted in Fig. 16. Unlike the convex edge structure with strong stiffness, the overall stiffness of the windshield plane is relatively weak, making it susceptible to significant structural deformation under the effect of the large overpressure. The included angle region mentioned above experiences a maximum overpressure of approximately 900 kPa at 4.82 ms. At this time, the response speed of the corresponding

structure of the windshield plane reaches 2.34 m/s, which is significantly higher than that of the unaffected area (0.92 m/s). As a result, the overpressure at the corresponding position of the FFICC is been increased by approximately 1 kPa compared to the region below with lower stiffness. For clarity, the nephograms at 4.82 ms are shown in Fig. 16.

In summary, it is evident that the formation of extreme shock wave overpressure on the local structure of the external surface of the CCTMH is not a sufficient factor for a significant increase in pressure wave overpressure in the corresponding region of the FFICC, as shown in Table 5. The presence of convex or concave features can have a detrimental impact on the FFICC. Therefore, it is crucial to ensure that the surrounding structure possesses sufficient stiffness to mitigate this adverse effect. This circumstance will inevitably lead to an increase in the weight of the CCTMH, which can negatively impact its overall performance. Hence, it is advisable to minimize or avoid incorporating convex or concave features as much as possible in the optimization design of the CCTMH to enhance its anti-shock wave performance.

4.2.2. Impacts of internal equipment and Inner cavity shape of the CCTMH

At about 2.3 ms, the muzzle blastfront reaches the CCTMH, resulting in a high-pressure region with a significant increase in overpressure, as shown in Fig. 17(a). In contrast, the overpressure isobars of the flow field show no visible changes when the pressure wave of the FFICC reaches the driver's position at 4.5 ms, as shown in Fig. 17(b).

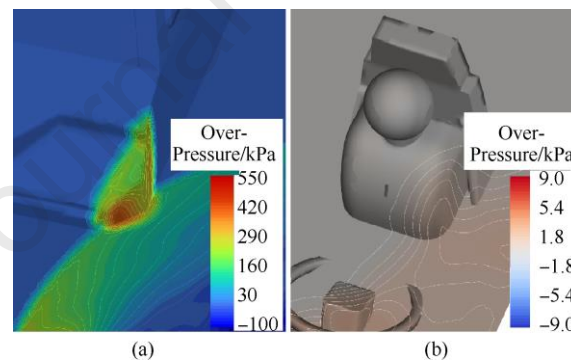


Fig. 17. The isobars distribution of FFOCC and FFICC. (a) FFOCC-2.3 ms; (b) FFICC-4.5 ms.

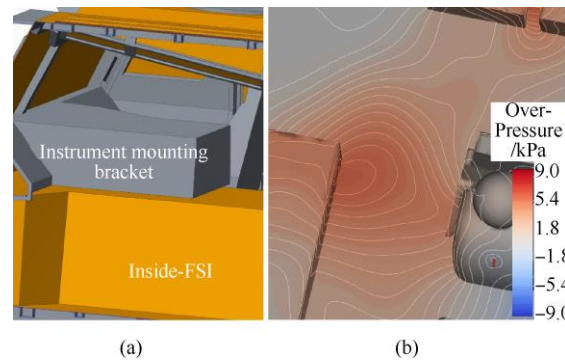


Fig. 18. Pressure wave of the FFICC forms relatively high-pressure region under the disturbance of the instrument support. (a) Instrument mounting bracket with a large cross-section; (b) FFICC-8 ms.

The propagation of the pressure wave in the FFICC is significantly disrupted by part of the instrument frame structures. This part of the instrument frame structure is connected with the bottom engine bulge area in Inside-FSI and has a large cross-section. At 8 ms, the maximum overpressure in the high-pressure region formed by reflecting and superimposing flow field pressure waves through the side facade of the instrument support approaches 5 kPa, as shown in Fig. 18. Combined with the analysis in section 4.1, it can be observed that even after the pressure wave completely skims over the FFICC (11.3 ms), the maximum overpressure peak of the FFICC continues to increase. For a certain period, the pressure wave is continuously reflected by Inside-FSI and continues to collide and superimpose with each other in the propagation process, while also receiving energy from the Str-CC. The energy derived from Str-CC is generated through the high-speed structural deformation caused by the FFOCC. Consequently, on the XY plane of the FFICC, the maximum overpressure peak approaches 9 kPa (as shown in Fig. 13(e)), which is significantly larger than the local overpressure peak induced by disturbances from the instrument support.

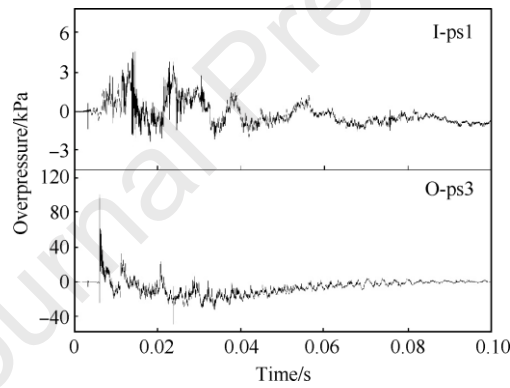


Fig. 19. Overpressure-time curve of the firing experiment at measuring points O-ps3 and I-ps1.

In contrast to the FFOCC, the closed nature of the CCTMH effectively avoids the high-intensity diffracted shock wave from the FFOCC. However, it also significantly retards the attenuation of pressure wave energy in the FFICC. Because the simulation calculation is constrained within a limited time, comparing firing data exceeding 100 ms allows for a clearer identification of the disparity in overpressure attenuation trends between the FFOCC and the FFICC. The overpressure of the FFICC maintains a large amplitude for an extended period after reaching its maximum peak, as evidenced by the measuring points O-ps3 and I-ps1, as shown in Fig. 19.

From the above comparative analysis, it can be observed that the shape of Inside-FSI, also the inner cavity shape of the CCTMH, plays a crucial role in influencing the development of pressure wave overpressure in the FFICC, compared to other internal equipment of the CCTMH such as seats and instrument supports. Consequently, it can be inferred that some ways effectively mitigate the impact of muzzle blast on the FFICC: reducing Str-CC energy supply to Inside-FSI and enhancing Str-CC absorption and attenuation efficiency toward the pressure wave

of the FFICC.

5. Conclusions

The response of the FFICC to overpressure under the muzzle blast is a double flow field problem involving structural coupling. To address this issue, a simulation solution strategy of distribution modeling and joint calculation was employed to establish a comprehensive numerical model. The model encompasses the entire path of shock wave propagation from the muzzle to the interior of the CCTMH under extreme firing condition ($0^{\circ}/-25^{\circ}$). Meanwhile, a systematic muzzle blast experiment was conducted. By analyzing simulation and experimental data, the formation and development patterns of the FFICC when subjected to extreme firing condition have been obtained. Additionally, the influences of the external structural characteristics, internal equipment, and inner cavity shape of the CCTMH on the overpressure distribution of the FFICC have been investigated. The main conclusions are as follows:

(1) It is reasonable to use a distributed modeling and joint simulation strategy to solve the problem of FFICC under the impact of the muzzle blast. The peak overpressure errors between numerical model results and experimental results are below 7% for the FFOCC, and below 15% for the FFICC, demonstrating that the numerical model effectively and accurately reflects the propagation process of the shock wave from the muzzle to the interior of the crew compartment.

(2) Overpressure characteristics of the FFICC: Due to attenuation caused by the Str-CC, the pressure wavefront of the FFICC significantly lags behind the shock wavefront of the FFOCC. Additionally, the maximum value of overpressure of the FFICC is a fraction of tens of that on the CCTMH external surface. In contrast to the FFOCC, the closed nature of the CCTMH significantly retards the attenuation of pressure wave energy in the FFICC, and the overpressure values demonstrate relatively moderate changes over time. The overpressure in the FFICC maintains a large amplitude for an extended period after reaching its maximum peak.

(3) Main influencing factors for overpressure of the FFICC: The frame-skin structure employed in the CCTMH helps to disperse the muzzle blast load and decrease the maximum overpressure peak within the FFICC. However, under the influence of the frame-skin structure, the formation and propagation trajectory of pressure waves in the FFICC become more intricate. The muzzle blast creates a high-amplitude overpressure at the convex or concave features on the external surface of the CCTMH. This significantly enhances the deformation rate and amount of the low-stiffness structure surrounding its convex or concave feature, leading to a significant augmentation in the overpressure of pressure waves at the corresponding location of the FFICC. In contrast, equipment such as the seats and instrument supports in the crew compartment has a negligible impact on the formation and development of the overpressure in the FFICC.

These conclusions provide specific guidance for optimizing the design of anti-shock wave structures for the CCTMH, considering internal flow field environments, and enhancing the comprehensive protective performance of the cab against muzzle blast. Furthermore, a foundation has been laid for relevant research on completing firing without truck-mounted howitzer operators leaving the cab.

Acknowledgements

This work was supported by the National Natural Science Foundation of China (Grant No. U2341269).

References

- [1] Qian LF, Xu YD, Chen LM. Design Theory and Methods of Vehicle-Mounted Howitzer. Beijing: Science Press; 2022.
- [2] Liao ZQ. Gas Dynamics of Automatic Weapons. Beijing: National Defense Industry Press; 2014.
- [3] Wei SC, Qian LF, Xu YD, Yin Q. Muzzle blast overpressure characteristics on the surface of vehicle-mounted howitzer's crew compartment. *Acta Armamentarii*. <https://doi.org/10.12382/bgxb.2023.0687>.
- [4] Li ZJ, Wang H, Chen CS, Jiang K. Numerical and experimental investigation into the evolution of the shock wave when a muzzle jet impacts a constrained moving body. *Def. Technol.* 2024; 33(3): 317–326.
- [5] Miao W, Yin Q, Qian LF. An approximate calculation method for ejection of propellant gas during after-effect period of artillery. *Acta Armamentarii* 2021; 42(7): 1381–1391.
- [6] Wang DY, Nan FQ, Liao X, Xiao ZL, Du P, Wang BB. Characteristics of muzzle flow of large caliber gun considering chemical reaction. *Acta Armamentarii* 2021; 42(8): 1624–1630.
- [7] Bai WB, Yu YG, Zhang XW. Numerical simulation of the underwater gun using gas-curtain launch. *Phys. Fluids* 2024; 36(3): 036128.
- [8] Sun QZ, Fan SW, Wang DR, Li JH. Numerical study of muzzle flow field of assault gun. *J. Ballist.* 2019; 31(4): 63–67.
- [9] Li PF, Zhang XB. Numerical research on adverse effect of muzzle flow formed by muzzle brake considering secondary combustion. *Def. Technol* 2021; 17(4): 1178–1189.
- [10] Li PF, Zhang XB. Numerical research on the impinging effect of sequential muzzle blast waves formed by successive shooting at high frequency. *Propellants Explo. Pyrotec.* 2020; 45(9): 1416–1427.
- [11] Sun ZQ, Li Q, Qu P, Lu L. Numerical investigation of the flame suppression mechanism of porous muzzle brake. *Phys. Fluids* 2023; 35(7): 075120.
- [12] Zhang HH, Chen ZH, Jiang XH, Han JL. Numerical simulation of the 3D flow fields of a muzzle brake and its efficiency calculation. *Acta Armamentarii* 2011; 32(5): 513–519.
- [13] Yu HW, Yuan JT, Wang ZH, Ge MR, Luo Y. Muzzle blast wave investigation and performance analysis of new-structure muzzle brake based on numerical simulation. *Chin. J. High Press. Phys.* 2020; 34(6): 101–111.
- [14] Li HZ, Jiang XH, Wang Y, Guo ZQ. *Intermediate Ballistics*. Beijing: Beijing Institute of Technology Press; 2014.
- [15] Zhuo CF, Feng F, Wu XS, Liu Q, Ma H. Numerical simulation of the muzzle flows with base bleed projectile based on dynamic overlapped grids. *Comput. Fluids* 2014; 105: 307–320.
- [16] Luo Y, Xu D, Li H. Analysis of the dynamic characteristics of the muzzle flow field and investigation of the influence of projectile nose shape. *Appl. Sci.* 2020; 10(4): 1468.

- [17]Lei HX, Zhao JL, Wang ZJ. Numerical simulation and experiments on muzzle blast overpressure in large-caliber weapons. *J. Eng. Sci. Technol. Rev.* 2016; 9(5): 111–116.
- [18]Guo ZQ, Wang Y, Jiang XH, Li HZ. Numerical study on effects of precursor flow on muzzle propellant flow field. *Acta Armamentarii* 2012; 33(6): 663–668.
- [19]Chen QK, Li PF, Zhou Q, Wang XF, Li M. Research on the measurement of muzzle shock wave pressure field for a naval gun. *IOP Conf. Ser. Earth Environ. Sci.* 2021; 791(1): 012096.
- [20]A. Moumen, B. Stirbu, J. Grossen, D. Laboureur, J. Gallant, P. Hendrick. Particle image velocimetry for velocity measurement of muzzle flow: Detailed experimental study. *Powder Technol.* 2022; 405: 117509.
- [21]Lai FW, Kong FS, Gao H, Liu YH. Design of distributed system for measuring muzzle blast wave based on LXI bus. *J. Ordnance Equip. Eng.* 2021; 42(9): 183–188.
- [22]V. Sekar, Q. H. Jiang, C. Shu, B. C. Khoo. Fast flow field prediction over airfoils using deep learning approach. *Phys. Fluids* 2019; 31(5): 057103.
- [23]C. Duru, H. Alemdar, O. U. Baran. A deep learning approach for the transonic flow field predictions around airfoils. *Comput. Fluids* 2022; 236: 105312.
- [24]N. T. T. Nguyen, G. R. Maskaly, A. S. Liao, C. L. Fryer, D. A. Shutt, V. P. Chiravalle, et al. Predicting shockwaves in radiograph images using different deep learning models. Presented at Applications of Machine Learning 2021. San Diego, California, USA: Aug; 2021. p. 112–123. (SPIE, 2021).
- [25]Hui XY, Bai JQ, Wang H, Zhang Y. Fast pressure distribution prediction of airfoils using deep learning. *Aerosp. Sci. Technol.* 2020; 105: 105949.
- [26]S. Bhatnagar, Y. Afshar, S. Pan, K. Duraisamy, S. Kaushik. Prediction of aerodynamic flow fields using convolutional neural networks. *Comput. Mech.* 2019; 64(2): 525–545.
- [27]Zhou MD, Qian LF, Cao CY, Chen GS, Kong J, Tong MH. Research on simulation of gun muzzle flow field empowered by artificial intelligence. *Def. Technol.* 2024; 32(2): 196–208.
- [28]Chen LM, Qian LF, Jiang K. Tiansient impact response analysis for cab of truck mounted howitzer under gun muzzle blast waves. *J. Ballist.* 2006; 18(1): 59–62.
- [29]Chen XY, Lu C, Sun WL, Li DY, Zhao XW, Zhou YB. Research on anti-shock wave cab structure design of a cannon. *Blasting* 2018; 35(3): 172–178.
- [30]Liu TH, Geng SG, Chen XD, S. Krajnovic. Numerical analysis on the dynamic airtightness of a railway vehicle passing through tunnels. *Tunn. Undergr. Sp. Tech.* 2020; 97(C): 103286.
- [31]Sun ZX, Yang GW, Zhu L. Study on the critical diameter of the subway tunnel based on the pressure variation. *Sci. China Technol. Sci.* 2014; 57(10): 2037–2043.
- [32]Zhou XX, Yin TJ, Li P, Chen L, Liu QH. Coupling study on key factors of interior pressure fluctuation of fuxing train. *J. Railw. Sci. Eng.* 2023; 20(6): 1974–1982.

[33]Wang QX, Hu ZL, Liang XF. Relationship among internal pressure, body air tightness and pressure of rail vehicle. *Journal of Traffic and Transportation Engineering* 2018; 18(4): 103–111.

[34]Feng YP, Chen CJ, Chen RT. Influence of vehicle body deformation on vehicle interior pressure under tunnel pressure based on flow-solid coupling. *Electr. Drive Locomot.* 2021; 3: 80–85.

[35]Zhuo CF, Yao WJ, Wu XS, Feng F, Xu P. Research on the muzzle blast flow with gas-particle mixtures based on Eulerian-Eulerian approach. *J. Mech.* 2016; 32(2): 185–195.

[36]Zhang XB, Jin ZM. *Interior Ballistics of Guns*. Beijing: Beijing Institute of Technology Press; 2014.

Journal Pre-proof

Conflict of Interest

The authors have no conflicts to disclose.

Journal Pre-proof